

Large magneto-optical effects in the van der Waals ferrimagnet $\text{Mn}_3\text{Si}_2\text{Te}_6$

Yuling Yin,^{1,2,3} Xiangang Wan^{1,2,4,5}, Xinhai Tu,^{1,2,*} and Di Wang^{1,2,†}

¹*National Laboratory of Solid State Microstructures and School of Physics, Nanjing University, Nanjing 210093, China*

²*Collaborative Innovation Center of Advanced Microstructures, Nanjing University, Nanjing 210093, China*

³*International Quantum Academy, Shenzhen 518048, China*

⁴*Hefei National Laboratory, Hefei 230088, China*

⁵*Jiangsu Physical Science Research Center, Nanjing University, Nanjing 210093, China*



(Received 27 April 2024; revised 21 July 2024; accepted 25 July 2024; published 4 September 2024)

Usually, traditional magneto-optical (MO) applications demand high magneto-optic figures of merit, which results in limited available materials. Tunable MO applications concerning polarization states and magnetic orientations have been proposed with the discovery of large MO effects in anisotropic low-dimensional materials. Recently, a van der Waals ferrimagnet $\text{Mn}_3\text{Si}_2\text{Te}_6$ exhibits colossal spin orientation-dependent magnetoresistance and magnetizability by comparing these properties between the in-plane ([100]) and out-of-plane ([001]) spin configurations. Thus exploring potential MO performances of $\text{Mn}_3\text{Si}_2\text{Te}_6$ in detail is of importance. By utilizing first-principles calculations together with group theory analyses, we systematically investigate the electronic, optical, and MO properties of $\text{Mn}_3\text{Si}_2\text{Te}_6$. An insulator-metal transition occurs between these two spin configurations. In addition, the maximal Kerr MO rotation angles of $\sim 0.41^\circ$ for the metal state are comparable to those of best-known MO materials, while the maximal Schäfer-Hubert rotation angle of the insulated state is nearly one-tenth. We find that the spin-orbital coupling on Te atoms makes a dominant contribution to the MO anisotropy. Based on the large MO performances and their tunability of magnetic orientation and intensity, we suggest that $\text{Mn}_3\text{Si}_2\text{Te}_6$ could serve as a promising MO material.

DOI: [10.1103/PhysRevB.110.104410](https://doi.org/10.1103/PhysRevB.110.104410)

I. INTRODUCTION

Magneto-optical (MO) effects are extensively used in a diverse range of applications, including isolators, circulators, modulators, sensors, and data storage devices [1–9], comprised mainly of first- and second-order MO effects. Herein, first-order MO effects are optical nonreciprocal, characterized by a linear dependence on magnetization, and their signs are odd in the direction of magnetization, involving the MO Faraday effect (MOFE) and MO Kerr effect (MOKE) [3–5, 10–18]. Second-order MO effects contain MO Schäfer-Hubert effect (MOSHE) and MO Voigt effect (MOVE) whose magnitudes are quadratic to the strength of magnetization and exhibit even sign behavior with respect to magnetization [15, 16, 19, 20]. The MOFE and MOVE effects refer to the rotation of the polarization planes of transmitted light in relation to the incident light, whereas MOKE and MOSHE effects pertain to the corresponding alterations in the polarization of reflected light compared to the incident light [14–16]. Usually, the MOKE and MOFE are used in polar geometry with normal light incidence and MOVE and MOSHE are given in longitudinal geometry.

Unfortunately, few materials are available in the traditional MO application field, since MO applications necessitate high MO rotation as well as low optical loss [21–26]. Up till now,

the most commonly employed material is the sage yttrium iron garnet ($\text{Y}_3\text{Fe}_5\text{O}_{12}$), which have been discovered decades ago [14, 22–33]. The applications of MO effects are still limited in three-dimensional isotopic optical conductivity, indicating small normal birefringence [14, 25, 34–37]. Exploration of different deflection behaviors of magneto-optic effects occurring at various polarization states remains very limited.

However, with the discovery of long-range magnetic orders and remarkable MO effects [17, 18, 38–41] in low-dimensional materials nowadays [42], traditional concepts have been broken and groundbreaking high-density MO and spintronic devices are emerging [26, 43–48]. On the one hand, low-dimensional materials process anisotropic optical absorption, indicating polarization-sensitive optical applications [5, 26, 43]. On the other hand, MO anisotropy (MOA), defined as the dependence of the off-diagonal part of the optical conductivity tensor [35, 49, 50], gives MO application prospects concerning magnetic directional dependence [44, 51–53]. Meanwhile, the operable spectral range is extended from the ultraviolet to the microwave regions indicating wider MO applications [26, 43].

Recently, a magnetic nodal-line semiconductor $\text{Mn}_3\text{Si}_2\text{Te}_6$ has been reported to show a uniquely continuously changing angular colossal magnetoresistance (CMR) [54–70]. This material exhibits an insulator-metal transition when magnetization orientation changes from in-plane to out-of-plane. A degenerated nodal-line band is pushed towards the Fermi surface by spin-orbital coupling (SOC) [57]. Since SOC is regarded as one of the causes of MO effects [1, 17], we suppose

*Contact author: tuxh@nju.edu.cn

†Contact author: diwang0214@nju.edu.cn

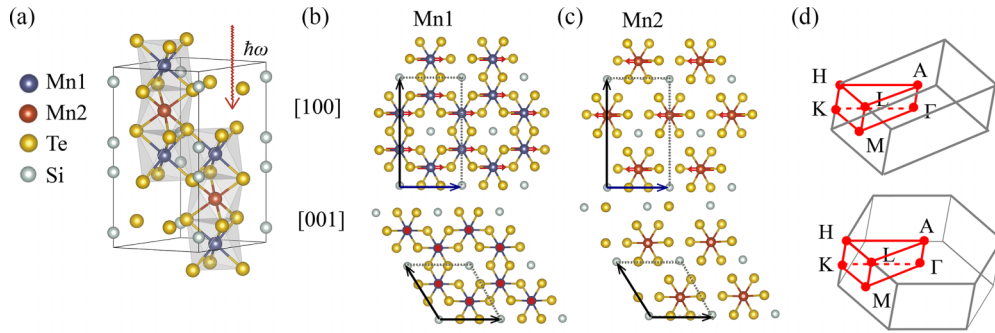


FIG. 1. Structures of $\text{Mn}_3\text{Si}_2\text{Te}_6$. (a) The hexagonal structure of $\text{Mn}_3\text{Si}_2\text{Te}_6$ is viewed along the $[110]$ direction. (b), (c) The vertical view of a single Mn1 [Mn2] honeycomb layer. The magnetic configurations along $[100]$ and $[001]$ axes belong to the orthogonal and hexagonal lattices, respectively. (d) Brillouin zone with high-symmetry points marked by red dots. The red arrow represents incident light along the z axis.

that $\text{Mn}_3\text{Si}_2\text{Te}_6$ have MO effects. Moreover, this material has three special features, so we suggest it would have some specific profits in optical integrated circuits fabrications. First, nanoflakes of this bulk self-intercalated van der Waals material $\text{Mn}_3\text{Si}_2\text{Te}_6$ can be mechanically exfoliated [71]. This is beneficial for $\text{Mn}_3\text{Si}_2\text{Te}_6$ to be integrated into van der Waals heterostructures to form field-effect devices [72,73]. Second, when applying an external magnetic field H , the in-plane saturation magnetization is easily satisfied, merely when $\mu_0 H \geq 0.05$ T [54]. Nevertheless, the out-of-plane magnetization increases gradually and only approaches the saturation magnetization at $\mu_0 H \geq 13$ T [54]. This means strong tunability of MO effects in terms of magnetic orientation and intensity. Third, the ground state of $\text{Mn}_3\text{Si}_2\text{Te}_6$ prefers in-plane magnetization, while some two-dimensional (2D) van der Waals materials with similar large Kerr rotations, such as CrI_3 , $\text{Cr}_2\text{Ge}_2\text{Te}_6$, and $\text{Fe}_3\text{Ge}_2\text{Te}_2$ [17,18,38–42,45,46], prefer out-of-plane magnetization. It denotes that $\text{Mn}_3\text{Si}_2\text{Te}_6$ could have potential MO applications at different external magnetic field orientations. Therefore, in the present work, based on first-principles calculations together with magnetic group analysis, we carry out $\text{Mn}_3\text{Si}_2\text{Te}_6$ optical and MO properties for both $[100]$ and $[001]$ spin configurations in full magnetization. We find that when the direction of normal incident light is fixed along the z axis, the Kerr maximal rotation angle for the metal state approaches $\sim 0.41^\circ$, comparable to those of best-known MO materials, and the MOSHE in an insulated state is nearly one-tenth in the case.

After this introduction, the paper unfolds as follows. Section II comprises a brief account of the crystal structure of $\text{Mn}_3\text{Si}_2\text{Te}_6$. Section III describes the optical and MO theory and employed calculation methods. Section IV presents the calculated results for electronic structures, magnetic properties, optical and MO conductivities, and MO effects. Section V contains the conclusions.

II. CRYSTAL STRUCTURES

$\text{Mn}_3\text{Si}_2\text{Te}_6$ crystallizes in a trigonal structure with a space group of $P\bar{3}1c$ (No. 163), where Mn has two inequivalent atomic positions [74,75], as shown in Fig. 1. Its ground state orders ferrimagnetically and the spin of Mn possesses a small canted configuration away from the a - b plane with a

ferrimagnetic Curie temperature $T_c = 78$ K [54,75,76]. For the $[001]$ magnetization, $\text{Mn}_3\text{Si}_2\text{Te}_6$ has a magnetic space group $P\bar{3}1c$ (No. 163.83, BNS setting). However, for the $[100]$ magnetization, it forms a magnetic space group $C2'/c'$ (No. 15.89, BNS setting). The primitive cells for them are shown in Figs. 1(b) and 1(c). Adjacent two Mn layers have antiparallel magnetizations for both in-plane and out-of-plane configurations. The lattice constants are given by $a = 7.029$ Å and $c = 14.255$ Å taken from Ref. [74] for the hexagonal lattice. All the crystal structures were visualized with the VESTA code [77].

III. OPTICAL AND MAGNETO-OPTICAL CALCULATION THEORY AND METHODS

We perform first-principles calculations using the linearized augmented plane-wave (LAPW) code WIEN2K [78], within the generalized gradient approximation (GGA) to account for the exchange-correlation interaction [79]. An $8 \times 8 \times 3$ centered k -point mesh was used to sample the material Brillouin zone. A denser mesh of $13 \times 13 \times 5$ was employed for the calculation of the dielectric tensor. Sphere radii of 2.5, 2.5, and 2.0 Bohr were chosen for Te, Mn, and Si, respectively. We adopt a local spin-density approximation (LSDA) as the exchange-correlation potential in all calculations [80]. The SOC is included using the second-order variational procedure [81]. The magnetic anisotropy energy (MAE) is calculated by combining force theorem and linear-response approach [82–85].

The independent elements of optical and MO conductivities can be formulated within the linear response theory, given by Kubo formula [86–89]. These conductivities are strictly restricted by lattice symmetries. In the $[001]$ spin configuration, the conductivity tensor σ containing both absorptive σ^{Ab} parts and dispersive σ^{Dis} parts is given by

$$\sigma = \begin{pmatrix} \sigma_{xx} & \sigma_{xy} & 0 \\ -\sigma_{xy} & \sigma_{xx} & 0 \\ 0 & 0 & \sigma_{zz} \end{pmatrix}. \quad (1)$$

In the [100] spin configuration, the conductivity tensor is given by

$$\sigma = \begin{pmatrix} \sigma_{xx} & \sigma_{xy} & \sigma_{xz} \\ -\sigma_{xy} & \sigma_{yy} & \sigma_{yz} \\ \sigma_{xz} & -\sigma_{yz} & \sigma_{zz} \end{pmatrix}. \quad (2)$$

Due to $C_{2y}T$ symmetry, σ_{xz} is symmetric and is different from σ_{xy} and σ_{yz} . For the interband contribution, through transition rules, the absorptive parts $\sigma_{\nu\mu}^{\text{Ab}}$ are given by [90–93]

$$\sigma_{\nu\mu}^{\text{Ab}}(\omega) = \frac{\pi e^2}{\hbar\omega m^2} \sum_{c,v} \int_{\text{BZ}} \frac{d\mathbf{k}}{(2\pi)^3} p_{cv}^{\nu} p_{vc}^{\mu} \times \delta(\epsilon_{\mathbf{k}c} - \epsilon_{\mathbf{k}v} - \hbar\omega), \quad (3)$$

where $\frac{\pi e^2}{\hbar\omega m^2}$ is a material specific constant and $\hbar\omega$ is the photon energy. p_{cv}^{ν} and p_{vc}^{μ} are the dipole matrix elements $\langle \mathbf{k}, c | p^{\nu} | \mathbf{k}, v \rangle$ and $\langle \mathbf{k}, v | p^{\mu} | \mathbf{k}, c \rangle$, respectively. ν and μ represent the coordinates. $|\mathbf{k}, c\rangle$ and $|\mathbf{k}, v\rangle$ represent conduction and valence electronic eigenstates, respectively. This would give the absorptive parts with both real $\sigma_{\nu\mu}^{1(\text{Ab})}(\omega)$ and imaginary $\sigma_{\nu\mu}^{2(\text{Ab})}(\omega)$ forms.

As indicated by Eq. (3), the diagonal absorptive components exclusively result in real forms. Concerning the off-diagonal absorptive components, $\sigma_{\nu\mu}^{1(\text{Ab})}(\omega)$ assumes a value of zero in materials exhibiting C_n symmetry, where $n = 3, 4, 6$. Consequently, in many discussions, only $\sigma_{\nu\mu}^{2(\text{Ab})}(\omega)$ pertains to the off-diagonal absorptive components [89,90,92,93]. In our analysis, the [001] spin configuration exhibits a threefold rotational symmetry, as discussed previously. Only the imaginary part of σ_{xy} means absorption. However, this symmetry (C_{3z}) is disrupted in the [100] spin configuration. Thus the real part of σ_{xz} and the imaginary parts of both σ_{yz} and σ_{xy} demonstrate characteristics associated with absorption.

The dispersive part $\sigma_{\nu\mu}^{\text{Dis}}$ of the conductivity tensor can be obtained from its corresponding absorptive using Kramers-Kronig transformation

$$\begin{aligned} \sigma_{\nu\mu}^{2(\text{Dis})}(\omega) &= -\frac{2\omega}{\pi} P \int_0^{\infty} \frac{\sigma_{\nu\mu}^{1(\text{Ab})}(\omega')}{\omega'^2 - \omega^2} d\omega', \\ \sigma_{\nu\mu}^{1(\text{Dis})}(\omega) &= \frac{2}{\pi} P \int_0^{\infty} \frac{\omega' \sigma_{\nu\mu}^{2(\text{Ab})}(\omega')}{\omega'^2 - \omega^2} d\omega', \end{aligned} \quad (4)$$

where P denotes the principal value. In the first row of Eq. (4), ν and μ may be equal or not, whereas in the second row of Eq. (4), ν and μ are not equal.

In this article, we fix the direction of normal incident light along the z axis. Then, due to the difference in magnetization direction, we show MOFE and MOKE for [001] spin configuration and MOVE and MOSHE for [100] spin configuration. For the reflected MOKEs and MOSHEs, we conduct them by solving the propagation Fresnel equation [94]

$$(n^2 \mathbf{1} - \boldsymbol{\epsilon} - \mathbf{n} : \mathbf{n}) \cdot \mathbf{E} = 0. \quad (5)$$

Here \mathbf{n} is the refractive index, \mathbf{E} is the electric field, and $\mathbf{n} : \mathbf{n}$ is the dyadic product. The dielectric tensor is given by $\boldsymbol{\epsilon} = 1 + \frac{4\pi i}{\omega} \boldsymbol{\sigma}$. By putting the refractive index and the electric field into the semi-infinite boundary conditions [95–97], the

MOKE can be given by

$$\Phi_K = \theta_K + i\eta_K = i \frac{n_+ - n_-}{1 - n_+ n_-} \quad (6)$$

and the MOSHE can be given by

$$\Phi_{SH} = \theta_{SH} + i\eta_{SH} = \frac{n_{\parallel} - n_{\perp}}{1 - n_{\parallel} n_{\perp}} \sin(2\alpha). \quad (7)$$

n_+ and n_- represent the refractive indices for left- and right-polarized lights, respectively. The refractive indices are related to the dielectric function via expressions $n_{\parallel} = \sqrt{\epsilon_{xx}}$ and $n_{\perp} = \sqrt{\epsilon_{yy} + \epsilon_{yz}^2 / \epsilon_{zz}}$. α is the angle between the electric field of incident light \mathbf{E} and magnetization direction. There are also some studies on the MO reflection effects of magnetic thin films on nonmagnetic substrates, generally finding that the magnitude of the rotation angle is enhanced [17,18,41,98,99]. This material can be mechanically exfoliated [71], making it beneficial for detecting thin film MO effects, which deserves further investigation. In contrast, the MOFEs and the MOVEs, due to attenuation during propagation, can only be detected in thin films, thereby encountering multiple internal reflection effects. But with normal incidence along the z axis [96,97], the MOFE and MOVE can be simplified as

$$\Phi_F = \theta_F + i\eta_F = \frac{\omega d}{2c} (n_+ - n_-) \quad (8)$$

and

$$\Phi_V = \theta_V + i\eta_V = \frac{\omega d}{2c} (n_{\parallel} - n_{\perp}) \sin(2\alpha), \quad (9)$$

respectively [1]. Henceforth, we set $\alpha = 45^\circ$ (s -wave plus p -wave incident lights with the same amplitudes) to get the maximal complex rotation angles.

Since there is an insulator-metal transition when spin orientation changes from in-plane to out-of-plane, we give an estimate of intraband contribution by using the Drude model [36,100,101]. In comparison with experimental measurements, we give the Drude conductivity as follows:

$$\sigma = \frac{\omega_p^2 \gamma}{4\pi(\omega^2 + \gamma^2)} - i \frac{\omega_p^2 \omega}{4\pi(\omega^2 + \gamma^2)}, \quad (10)$$

where ω_p is the plasma frequency and $\gamma = 0.01$ eV is the carrier scattering rate by fitting our real conductivities to experimental zero-frequency conductivity in order of 0.01×10^{15} Hz (~ 10 S/cm) [54,57,58]. The plasma frequency is given by [101]

$$\omega_p^2 = \frac{\hbar^2 e^2}{\pi m^2} \sum_n \int_{\mathbf{k}} |\langle \psi_{n,\mathbf{k}} | \mathbf{p} | \psi_{n,\mathbf{k}} \rangle|^2 \delta(E_{n,\mathbf{k}} - E_F) d\mathbf{k}. \quad (11)$$

IV. RESULTS AND DISCUSSIONS

A. Magnetic properties and electronic structures

The valence of Mn^{2+} ions is in a $3d^5$ configuration, leading to quenched orbital moments, predicted in favor of antiferromagnetic couplings [54,75,76,102,103]. However, $\text{Mn}_3\text{Si}_2\text{Te}_6$ is found to be ferrimagnetic, with an intralayer ferromagnetic and interlayer antiferromagnetic configuration in previous

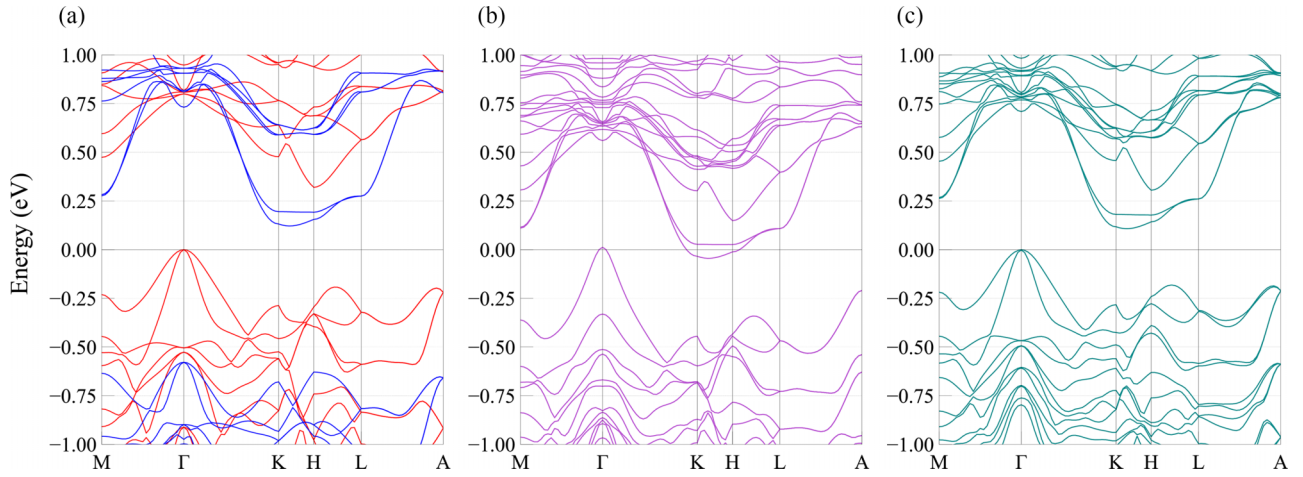


FIG. 2. Band structures of $\text{Mn}_3\text{Si}_2\text{Te}_6$. (a) Scalar-relativistic electronic band structure of $\text{Mn}_3\text{Si}_2\text{Te}_6$, where the red [blue] line represents the spin-up [spin-down] state. (b), (c) Electronic band structures of $\text{Mn}_3\text{Si}_2\text{Te}_6$ in the out-of-plane [in-plane] spin configuration with SOC. The paths in electric band structures in planes correspond to the Brillouin zone in Fig. 1(d).

research. This is a result of the inherent frustration owing to the third-nearest-neighbor coupling over the second-nearest-neighbor coupling [75,103]. For both [100] and [001] spin configurations, our calculated spin moments are almost the same, with $4.296\mu_B$ for Mn1 irons and $4.158\mu_B$ for Mn2 irons, corresponding to experimental results [75,76]. The orbital moments are quite different. In the [001] spin configuration, the orbital moments of Mn1 and Mn2 are the same ($0.021\mu_B$), while, in the [100] spin configuration, the orbital moments of Mn1 ($0.035\mu_B$) and Mn2 ($0.046\mu_B$) differ by $\sim 0.01\mu_B/\text{Mn}$. Furthermore, the calculated MAE ($\Delta E = E^{[001]} - E^{[100]} = 0.706 \text{ meV/Mn}$) is in agreement with experimental observations [75,77]. To better understand the electric, optical, and MO properties of $\text{Mn}_3\text{Si}_2\text{Te}_6$, we present the calculated electronic band structures in Fig. 2. Except for a significant band spitting at Γ point around the Fermi surface, we can see that these band structures are essentially the same. This similarity leads to the optical conductivities in the group state [100] spin configuration being almost the same as those in the [001] spin configuration. $\text{Mn}_3\text{Si}_2\text{Te}_6$ in the ground state of the [100] spin configuration is an indirect band-gap semiconductor with a 0.152 eV band gap, while it becomes a full-gapped metal in the [001] spin configuration [57], leading to intraband Drude conductivities.

Then we present the total as well as site-, spin-, and orbital-projected density of states (DOS) spectra of $\text{Mn}_3\text{Si}_2\text{Te}_6$ in Fig. 3. We can see that d orbitals of Mn are highly hybridized with p orbitals of Te. The lower valence bands ranging from -4.2 to -2.0 eV and the lower conduction band ranging from 0.0 to 2.0 eV are dominated by d orbitals of Mn together with a minor contribution of p orbitals of Te. Near the Fermi surface, p orbitals of Te contribute a bit more than the d orbitals of Mn to the upper valence bands ranging from -2.0 to 0.0 eV. The local DOS of Mn1 and Mn2 sites are rather different. The DOS of Mn1 shows two significant peaks in the valence range, while the DOS of Mn2 shows a rather dispersive pattern. In spin [001] configuration, the $d_{x^2-y^2}$, d_{xy} , and d_{z^2} orbitals projected DOS of Mn2 peaks are very shaped and located at 0.63 eV and 0.88 eV, respectively. In spin [100] configuration, the major DOS contributions come from $d_{x^2-y^2}$, d_{xy} with an

orbital projected DOS peak at 1.0 eV, while the peak of d_{z^2} is down to a quarter of that in spin [001] configuration.

B. Optical conductivities

We present the calculated interband optical conductivities from Eq. (3) for $\text{Mn}_3\text{Si}_2\text{Te}_6$ in Figs. 4(a) and 4(b). Overall, diagonal optical spectra for both configurations are very smooth without any pronounced peaks, which results from the equally intense band structures. Besides, we can see that these two optical spectra are similar and consistent with the similarity among electronic structures we discussed before. The real parts start to increase steadily from the absorption edge ~ 0.2 eV due to the existence of the band gap at Γ point.

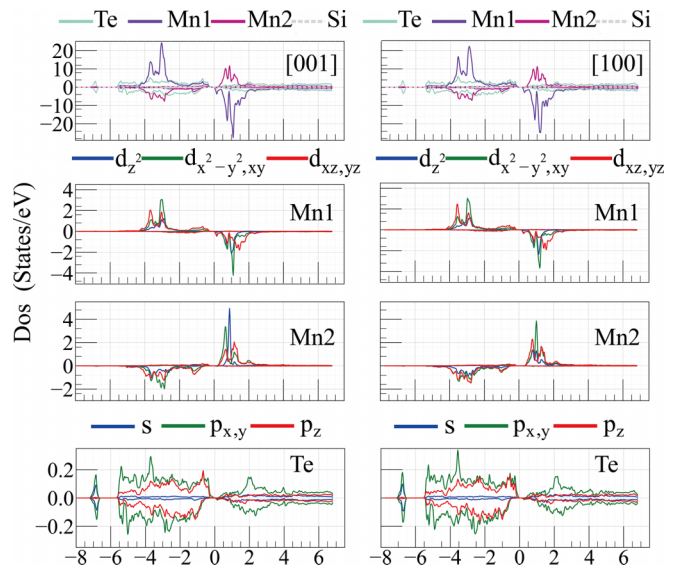


FIG. 3. Density of states. The relativistic DOS is calculated using LSDA+SOC. The Fermi level is set at 0 eV. The two subfigures in the first row plot the total density of states of each atom. The positive density of states corresponds to spin-up, while the negative density of states corresponds to spin-down. The left and right panels are the density of states for [001] and [100] spin configurations, respectively.

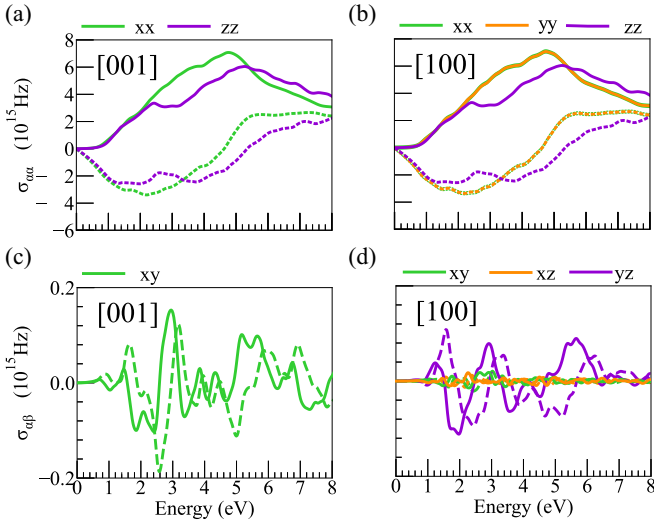


FIG. 4. Optical and MO conductivities. (a), (b) Diagonal conductivities and (c), (d) off-diagonal conductivities (b), (d) for in-plane and (a), (c) for out-of-plane spin configurations, respectively. All the spectra have been convoluted with a Lorentzian of 0.1 eV to simulate the finite electron lifetime effects. Solid and dashed lines represent real and imaginary components of the conductivity tensor, respectively.

Interestingly, there is almost no difference between the real diagonal conductivity σ_{xx}^1 and σ_{zz}^1 in the low-energy region of 0.2 eV to 2.4 eV, indicating little optical anisotropy. The decline of σ_{zz}^1 at 2.4 eV is suggested by a large band gap at Γ to A from ~ 2.0 eV to ~ 2.4 eV, which is not shown in our figures. In the meantime, σ_{xx}^1 still increases steadily from ~ 2.4 eV to ~ 5.2 eV, resulting in σ_{xx}^1 becoming larger than σ_{zz}^1 in this region. Later, they decrease steadily after σ_{xx}^1 and σ_{zz}^1 reach maximum optical conductivities at ~ 4.8 eV and ~ 5.2 eV, respectively.

We can associate the partial density of states shown with optical absorption by the absorptive conductivity equation. With attention to that the $p_{x,y}$ and $d_{x^2-y^2,xy}$ (p_z and d_{z^2}) can only be excited by $E \perp c$ ($E \parallel c$), while the $d_{xy,yz}$ can be excited by both. σ_{xx} and σ_{zz} , which means optical anisotropy in the high energy range of ~ 2.4 eV to ~ 5.2 eV, can be further understood by the weight of Mn $d_{x^2-y^2,xy}$ orbitals becoming larger than that of d_{z^2} orbitals in the density of state ranging from ~ -5.0 eV to ~ -2.0 eV and Te $p_{x,y}$ orbitals becoming larger than that of p_z orbitals ranging from ~ 1.0 eV to ~ 3.0 eV, while these components are close and small ranging from ~ -1.5 eV to ~ 1.0 eV. When the optical frequency becomes larger, σ_{zz} exceeds σ_{xx} , although the overall weight of p_x and d_{xy,x^2-y^2} is still larger than p_z and d_{z^2} . This might be explained by the significant $d_{xy,yz}$ states.

Towards intraband contribution, our calculated diagonal plasma frequencies are given by 0.0599 eV and 0.0431 eV for ω_p^{xx} and ω_p^{zz} , which are very tiny compared with those for common metals, such as $(4.9 + i1.8\pi)$ eV for iron, $(8.3 + i2\pi)$ eV for cobalt, and $(7.5 + i2.24\pi)$ eV for nickel [104]. This can be seen from the band structures; the intraband contributions are very small due to very few Fermi surface pockets. The smaller the scattering rate γ is, the more scattering is in the metal state (Fig. 5). When ω comes close to 0.05 eV, intraband conduc-

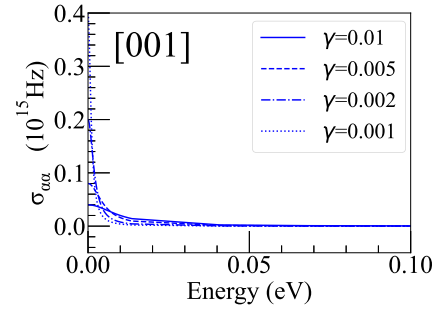


FIG. 5. Drude optical conductivity within 0.1 eV.

tivity decreases to the order of 10^{10} Hz for $\gamma = 0.01$ eV. In all these estimations, all Drude conductivities are very small compared with interband optical conductivities.

C. Magneto-optical conductivities

The calculated off-diagonal parts are displayed in Fig. 4. We can see that σ_{xy} and σ_{xz} are tiny compared with σ_{yz} in [100] spin configuration, although they are all allowed by symmetry. The overall features of spectra σ_{xy} in [001] spin configuration and σ_{yz} in [100] spin configuration are similar. They oscillate significantly with several high peaks and are in similar growth and decline trends. Specifically, for the real parts, prominent peaks occur around 2.0, 2.9, and 5.5 eV. On the other hand, the imaginary parts have pronounced peaks around 1.6, 2.6, 3.2, and 5.0 eV. A major difference is the peak at around 2.9 eV of the real parts in the in-plane spin configuration reduces to half of that in the out-of-plane one.

Furthermore, we also give MOA in Fig. 6 to inform more relation about MO conductivity between two spin configurations by turning on/off SOC on different equivalent atoms [50]. When we turn off the SOC on Te atoms, the strong suppression marked by green lines can be found, indicating that Te atoms' SOC strongly affects the off-diagonal optical conductivities and is mainly responsible for the large MO anisotropy.

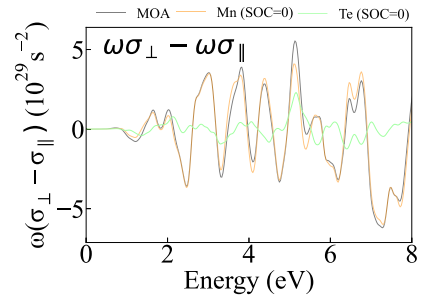


FIG. 6. Magneto-optical anisotropy. Calculated absorptive off-diagonal part of MO anisotropy together with the results of the calculations for the SOC set to zero on different equivalent atom sites. σ_{\perp} represents σ_{xy} in out-of-plane configuration and σ_{\parallel} represents σ_{yz} in in-plane configuration.

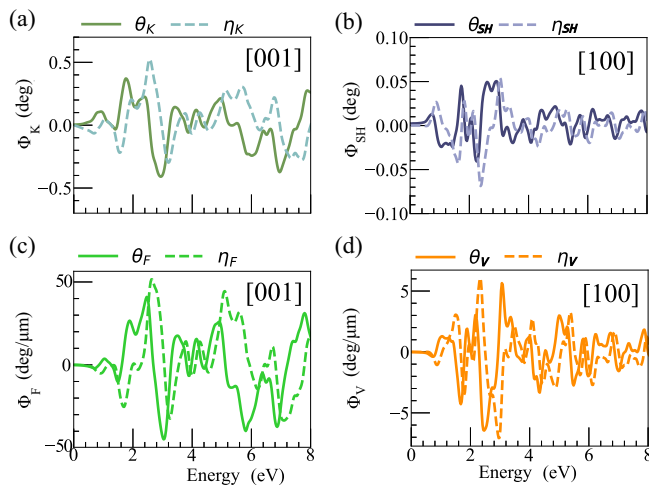


FIG. 7. Magneto-optical effect. (a), (b) MOKE [MOSHE] and (c), (d) MOFE [MOVE] for out-of-plane [in-plane] spin configuration with the normal incidence in the case of the x - z incidence plane.

D. Magneto-optical effects

Finally, we study MO effects in $\text{Mn}_3\text{Si}_2\text{Te}_6$ and plot complex rotation angles as a function of photon energy in Fig. 7 when the direction of normal incident light is fixed along the z axis. Overall, the MO effect in [001] spin configuration is nearly ten times larger than that in another configuration, indicating a potential application in the adjustable spatial resolution aspect. The MO effects of the former mainly arise from the first-order MOKEs and MOFEs, while the MO effects of the latter mainly arise from the second-order MOSHEs and MOVEs. When rotation crosses the zero line with a positive/negative slope, a valley/peak turns up in the corresponding ellipticity spectrum, and vice versa, which is ascribed to the Kramers-Kronig relation. The positive Kerr rotation maximum ($\sim 0.37^\circ$) for [001] spin configuration occurs at ~ 1.8 eV, while the positive Schäfer-Hubert (SH) rotation maximum ($\sim 0.05^\circ$) for [100] spin configuration appears at ~ 2.6 and ~ 2.9 eV. The negative Kerr rotation maximum ($\sim 0.41^\circ$) for [001] spin configuration occurs at ~ 2.9 eV, while the negative SH rotation maximum ($\sim 0.04^\circ$) for [100] spin configuration appears at ~ 2.2 eV. Similarly, the positive/negative Kerr ellipticity maximum ($\sim 0.52^\circ / \sim 0.3^\circ$) for [001] spin configuration occurs at $\sim 2.6 / \sim 3.2$ eV, while the SH ellipticity maximum ($\sim 0.054^\circ / \sim 0.069^\circ$) for [100] spin configuration appears at $\sim 3.0 / \sim 2.4$ eV. As a comparison, we list the Kerr rotation angles of other known MO materials. In particular, widely used ferromagnetic semiconductors $\text{Y}_3\text{Fe}_5\text{O}_{12}$ and $\text{Bi}_3\text{Fe}_5\text{O}_{12}$ in spintronic research have Kerr rotation angles of -0.12° at 4.8 eV and -1.21° at 2.4 eV, respectively [89], while the largest Kerr rotation of $\sim 0.41^\circ$ occurs at ~ 2.9 eV for $\text{Mn}_3\text{Si}_2\text{Te}_6$. Diluted magnetic semiconductors $\text{Ga}_{1-x}\text{Mn}_x\text{As}$ were reported to show a Kerr rotation angle as large as 0.4° at 1.80 eV [105]. MnBi thin films have a larger Kerr rotation angle of 2.3° [106]. The concurrence of large and small MO effects in $\text{Mn}_3\text{Si}_2\text{Te}_6$ may have promising potential applications in high-density MO devices and MO nanosensors with adjustable spatial resolution.

As the complex rotation angles of reflected light introduced above, the highest peak of the Faraday rotation angle of transmitted light $41^\circ/\mu\text{m}$ occurs at 2.46 eV, and the lowest valley $45^\circ/\mu\text{m}$ appears at 3.03 eV for [001] spin configuration. However, the highest peak of the Voigt rotation angle $5.6^\circ/\mu\text{m}$ occurs at 3.06 eV and the lowest valley $6.5^\circ/\mu\text{m}$ appears at 2.46 eV for [100] spin configuration. For ellipticity, the Faraday highest peak $52^\circ/\mu\text{m}$ occurs at 2.63 eV and the Faraday lowest valley $32^\circ/\mu\text{m}$ appears at 3.25 eV for [001] spin configuration, while the Voigt highest peak $6.1^\circ/\mu\text{m}$ occurs at 2.33 eV and the Voigt lowest valley $7.1^\circ/\mu\text{m}$ appears at 2.95 eV for [100] spin configuration. As a contrast, MnBi films possess very large Faraday rotation angles of $\sim 80^\circ/\mu\text{m}$ at 1.8 eV [106]. $\text{Y}_3\text{Fe}_5\text{O}_{12}$ and $\text{Bi}_3\text{Fe}_5\text{O}_{12}$ have Faraday rotations of $7.2^\circ/\mu\text{m}$ at 3.9 eV and $51.2^\circ/\mu\text{m}$ at 3.7 eV, respectively [89].

V. CONCLUSIONS

In summary, we systematically study the electronic, optical, and MO properties of $\text{Mn}_3\text{Si}_2\text{Te}_6$. It is an indirect band-gap semiconductor in the ground state with [100] spin configuration, while it becomes a full-gapped metal in the [001] spin configuration. Although static conductivity shows a CMR effect [54–58], in the interband energy range, the similarity of band structures leads to similar optical conductivities. Beyond that, based on experimental measurements [54] and our calculated plasma frequencies, we show the Drude conductivity in metal state originating from intraband contribution is relatively small. When the direction of normal incident light is fixed along the z axis, the maximal Kerr rotation angle for the metal state approaches $\sim 0.41^\circ$. Notably, it is comparable to that of the well-known materials explicitly referenced before, suggesting compelling prospects for leveraging these materials in MO sensors and high-density MO data-storage devices [14,17,18,22–33,38–42,45,46]. SHMOE in an insulated state is nearly one-tenth in the case. When the direction of normal incident light is to the x axis, the Kerr MO effect in the insulated state is as large as in the metal state as expected. We also investigate the MO anisotropy and show the significance of SOC of Te atoms. The large rotation angle of $\text{Mn}_3\text{Si}_2\text{Te}_6$, plus other interesting physical properties such as CMR, magnetic phase transition, and MOA, would make this material an exciting platform in spintronic and high-density MO nanodevices.

ACKNOWLEDGMENTS

This work was financially supported by the National Natural Science Foundation of China (Grants No. 12188101, No. 12334007, and No. 12474233), the National Key R&D Program of China (Grant No. 2022YFA1403601), Innovation Program for Quantum Science and Technology (Grants No. 2021ZD0301902 and No. 2024ZD0300101), Natural Science Foundation of Jiangsu Province (No. BK20233001, BK20243011), and the China Postdoctoral Science Foundation (Grant No. 2023M731615). This work was also supported by the New Cornerstone Science Foundation through the XPLOER PRIZE.

- [1] V. Antonov, B. Harmon, and A. Yaresko, *Electronic Structure and Magneto-optical Properties of Solids* (Springer Science & Business Media, New York, 2004).
- [2] É. du Trémolet de Lacheisserie, D. Gignoux, and M. Schlenker, Magneto-optical effects, in *Magnetism* (Springer, New York, 2002), pp. 399–442.
- [3] L. Fan, J. Wang, L. T. Varghese, H. Shen, B. Niu, Y. Xuan, A. M. Weiner, and M. Qi, *Science* **335**, 447 (2012).
- [4] L. Bi, J. Hu, P. Jiang, D. H. Kim, G. F. Dionne, L. C. Kimerling, and C. Ross, *Nat. Photon.* **5**, 758 (2011).
- [5] T. Zaman, X. Guo, and R. Ram, *Appl. Phys. Lett.* **90**, 023514 (2007).
- [6] F. Koppens, T. Mueller, P. Avouris, A. Ferrari, M. Vitiello, and M. Polini, *Nat. Nanotechnol.* **9**, 780 (2014).
- [7] F. Bonaccorso, Z. Sun, T. Hasan, and A. Ferrari, *Nat. Photon.* **4**, 611 (2010).
- [8] J. Fujita, M. Levy, R. M. Osgood, Jr., L. Wilkens, and H. Dötsch, *Appl. Phys. Lett.* **76**, 2158 (2000).
- [9] C. L. Hogan, *Rev. Mod. Phys.* **25**, 253 (1953).
- [10] F. D. M. Haldane and S. Raghu, *Phys. Rev. Lett.* **100**, 013904 (2008).
- [11] W.-K. Tse and A. H. MacDonald, *Phys. Rev. Lett.* **105**, 057401 (2010).
- [12] R. L. Espinola, T. Izuhara, M.-C. Tsai, R. M. Osgood, and H. Dötsch, *Opt. Lett.* **29**, 941 (2004).
- [13] X. Luo, M. Zhou, J. Liu, T. Qiu, and Z. Yu, *Appl. Phys. Lett.* **108**, 131104 (2016).
- [14] F. J. Kahn, P. Pershan, and J. Remeika, *Phys. Rev.* **186**, 891 (1969).
- [15] P. Yang, W. Feng, X. Zhou, X. Yang, and Y. Yao, *Phys. Rev. B* **106**, 174427 (2022).
- [16] X. Yang, P. Yang, X. Zhou, W. Feng, and Y. Yao, *Phys. Rev. B* **106**, 054408 (2022).
- [17] M.-C. Jiang and G.-Y. Guo, *Phys. Rev. B* **105**, 014437 (2022).
- [18] Y. Fang, S. Wu, Z.-Z. Zhu, and G.-Y. Guo, *Phys. Rev. B* **98**, 125416 (2018).
- [19] H. C. Mertins, P. M. Oppeneer, J. Kuneš, A. Gaupp, D. Abramsohn, and F. Schäfers, *Phys. Rev. Lett.* **87**, 047401 (2001).
- [20] S. Valencia, A. Kleibert, A. Gaupp, J. Ruzs, D. Legut, J. Bansmann, W. Gudat, and P. M. Oppeneer, *Phys. Rev. Lett.* **104**, 187401 (2010).
- [21] J. Smet, L. Peng, Y. Hirayama, and C. Fonstad, *Appl. Phys. Lett.* **64**, 986 (1994).
- [22] M. Nur-E-Alam, M. Vasiliev, and K. Alameh, *Coatings* **12**, 1471 (2022).
- [23] L. Seravalli and F. Sacconi, *J. Phys.: Mater.* **3**, 042005 (2020).
- [24] H. Dötsch, N. Bahlmann, O. Zhuromskyy, M. Hammer, L. Wilkens, R. Gerhardt, P. Hertel, and A. F. Popkov, *J. Opt. Soc. Am. B* **22**, 240 (2005).
- [25] M. N. Deeter, A. Rose, and G. W. Day, *J. Lightwave Technol.* **8**, 1838 (1990).
- [26] S. Kharratian, H. Urey, and M. C. Onbaşlı, *Adv. Opt. Mater.* **8**, 1901381 (2020).
- [27] M. R. Nurrahman, D. Kim, M.-K. Seo, and A. A. Iskandar, *J. Nonlin. Opt. Phys. Mater.* **28**, 1950043 (2019).
- [28] S. Tomita, T. Kato, S. Tsunashima, S. Iwata, M. Fujii, and S. Hayashi, *Phys. Rev. Lett.* **96**, 167402 (2006).
- [29] M. Inoue and T. Fujii, *J. Appl. Phys.* **81**, 5659 (1997).
- [30] M. C. Onbasli, L. Beran, M. Zahradník, M. Kučera, R. Antoš, J. Mistrík, G. F. Dionne, M. Veis, and C. A. Ross, *Sci. Rep.* **6**, 23640 (2016).
- [31] G.-M. Yang, J. Wu, J. Lou, M. Liu, and N. X. Sun, *IEEE Trans. Magn.* **49**, 5063 (2013).
- [32] Y. Okada, D. Tamura, K. Kobayashi, and H. Yokoi, *Jpn. J. Appl. Phys.* **54**, 092202 (2015).
- [33] S. Wittekoek, T. J. Popma, J. Robertson, and P. Bongers, *Phys. Rev. B* **12**, 2777 (1975).
- [34] J. A. Arregi, P. Riego, and A. Berger, *J. Phys. D* **50**, 03LT01 (2017).
- [35] G. Y. Guo and H. Ebert, *Phys. Rev. B* **50**, 10377 (1994).
- [36] G. Y. Guo and H. Ebert, *Phys. Rev. B* **51**, 12633 (1995).
- [37] G. Y. Guo and H. Ebert, *J. Magn. Magn. Mater.* **156**, 173 (1996).
- [38] M. Wu, Z. Li, T. Cao, and S. G. Louie, *Nat. Commun.* **10**, 2371 (2019).
- [39] Y. Okamura, S. Minami, Y. Kato, Y. Fujishiro, Y. Kaneko, J. Ikeda, J. Muramoto, R. Kaneko, K. Ueda, V. Kocsis *et al.*, *Nat. Commun.* **11**, 4619 (2020).
- [40] Y. D. Kato, Y. Okamura, S. Minami, R. Fujimura, M. Mogi, R. Yoshimi, A. Tsukazaki, K. S. Takahashi, M. Kawasaki, R. Arita *et al.*, *npj Quantum Mater.* **7**, 73 (2022).
- [41] V. Kumar Gudelli and G.-Y. Guo, *New J. Phys.* **21**, 053012 (2019).
- [42] C. Gong, L. Li, Z. Li, H. Ji, A. Stern, Y. Xia, T. Cao, W. Bao, C. Wang, Y. Wang *et al.*, *Nature (London)* **546**, 265 (2017).
- [43] S. Jiang, L. Li, Z. Wang, K. F. Mak, and J. Shan, *Nat. Nanotechnol.* **13**, 549 (2018).
- [44] Z. Sun, A. Martinez, and F. Wang, *Nat. Photon.* **10**, 227 (2016).
- [45] A. K. Geim and I. V. Grigorieva, *Nature (London)* **499**, 419 (2013).
- [46] B. Huang, G. Clark, E. Navarro-Moratalla, D. R. Klein, R. Cheng, K. L. Seyler, D. Zhong, E. Schmidgall, M. A. McGuire, D. H. Cobden *et al.*, *Nature (London)* **546**, 270 (2017).
- [47] H. Yuan, X. Liu, F. Afshinmanesh, W. Li, G. Xu, J. Sun, B. Lian, A. G. Curto, G. Ye, Y. Hikita *et al.*, *Nat. Nanotechnol.* **10**, 707 (2015).
- [48] D. Li, H. Jussila, L. Karvonen, G. Ye, H. Lipsanen, X. Chen, and Z. Sun, *Sci. Rep.* **5**, 15899 (2015).
- [49] V. N. Antonov, L. Uba, S. Uba, A. Yaresko, A. Y. Perlov, and V. Nemoshkalenko, *Low Temp. Phys.* **27**, 425 (2001).
- [50] L. Uba, S. Uba, V. N. Antonov, A. N. Yaresko, T. Ślęzak, and J. Korecki, *Phys. Rev. B* **62**, 13731 (2000).
- [51] F. Bentivegna, M. Nyvlt, J. Ferre, J. Jamet, A. Brun, S. Visnovsky, and R. Urban, *J. Appl. Phys.* **85**, 2270 (1999).
- [52] R. Vincent and R. Carminati, *Phys. Rev. B* **83**, 165426 (2011).
- [53] A. Lampis, R. Culver, B. Megyeri, and J. Goldwin, *Opt. Express* **24**, 15494 (2016).
- [54] Y. Ni, H. Zhao, Y. Zhang, B. Hu, I. Kimchi, and G. Cao, *Phys. Rev. B* **103**, L161105 (2021).
- [55] Y. Liu, Z. Hu, M. Abeykoon, E. Stavitski, K. Attenkofer, E. D. Bauer, C. Petrovic *et al.*, *Phys. Rev. B* **103**, 245122 (2021).
- [56] J. Wang, S. Wang, X. He, Y. Zhou, C. An, M. Zhang, Y. Zhou, Y. Han, X. Chen, J. Zhou *et al.*, *Phys. Rev. B* **106**, 045106 (2022).
- [57] J. Seo, C. De, H. Ha, J. E. Lee, S. Park, J. Park, Y. Skourski, E. S. Choi, B. Kim, G. Y. Cho *et al.*, *Nature (London)* **599**, 576 (2021).

- [58] Y. Zhang, Y. Ni, H. Zhao, S. Hakani, F. Ye, L. DeLong, I. Kimchi, and G. Cao, *Nature (London)* **611**, 467 (2022).
- [59] C. Ran, X. Mi, J. Shen, H. Wang, K. Yang, Y. Liu, G. Wang, G. Wang, Y. Shi, A. Wang *et al.*, *Phys. Rev. B* **108**, 125103 (2023).
- [60] Z. Zhang, G. Liu, W. Qi, H. Xie, J. Guo, Y. Du, T. Wang, H. Zhang, F. Zhou, J. Li *et al.*, *AIP Adv.* **14**, 035238 (2024).
- [61] R. Olmos, P.-H. Chang, P. Mishra, R. R. Zope, T. Baruah, Y. Liu, C. Petrovic, and S. R. Singamaneni, *J. Phys. Chem. C* **127**, 10324 (2023).
- [62] Q. Li, Y. Cheng, D. Zhao, Y. Huang, X. Wan, and J. Zhou, *New J. Phys.* **25**, 103020 (2023).
- [63] S. W. Lovesey, *Phys. Rev. B* **107**, 224410 (2023).
- [64] C. Tan, M. Deng, Y. Yang, L. An, W. Ge, S. Albarakati, M. Panahandeh-Fard, J. Partridge, D. Culcer, B. Lei *et al.*, *Nano Lett.* **24**, 4158 (2024).
- [65] S. D. Mijin, A. Šolajić, J. Pešić, Y. Liu, C. Petrovic, M. Bockstedte, A. Bonanni, Z. V. Popović, and N. Lazarević, *Phys. Rev. B* **107**, 054309 (2023).
- [66] C. Bigi, L. Qiao, C. Liu, P. Barone, M. C. Hatnean, G.-R. Siemann, B. Achinuq, D. A. Mayoh, G. Vinai, V. Polewczyk, D. Dagur, F. Mazzola, P. Bencok, T. Hesjedal, G. van der Laan, W. Ren, G. Balakrishnan, S. Picozzi, and P. D. C. King, *Phys. Rev. B* **108**, 054419 (2023).
- [67] C. I. Kwon, K. Kim, S. Y. Kim, R. A. Susilo, B. Kang, K. Kim, D. Y. Kim, J. Kim, B. Kim, and J. S. Kim, *Curr. Appl. Phys.* **53**, 51 (2023).
- [68] Q. Wu, Q. Yin, S. Zhang, T. Hu, D. Wu, L. Yue, B. Li, S. Xu, R. Li, Q. Liu *et al.*, *Adv. Opt. Mater.* **12**, 2301863 (2023).
- [69] R. Olmos, J. A. Delgado, H. Iturriaga, L. M. Martinez, C. L. Saiz, L. Shao, Y. Liu, C. Petrovic, and S. R. Singamaneni, *J. Appl. Phys.* **130**, 013902 (2021).
- [70] L. Qiao, P. Barone, B. Yang, P. D. King, W. Ren, and S. Picozzi, *Phys. Chem. Chem. Phys.* **26**, 8604 (2024).
- [71] Y. Lu, Z. Zhou, X. Kan, Z. Yang, H. Deng, B. Liu, T. Wang, F. Liu, X. Liu, S. Zhu *et al.*, *Nanomaterials* **13**, 602 (2023).
- [72] Z. Wang, I. Gutiérrez-Lezama, N. Ubrig, M. Kroner, M. Gibertini, T. Taniguchi, K. Watanabe, A. Imamoğlu, E. Giannini, and A. F. Morpurgo, *Nat. Commun.* **9**, 2516 (2018).
- [73] N. Maccaferri, X. Inchausti, A. García-Martín, J. C. Cuevas, D. Tripathy, A. O. Adeyeye, and P. Vavassori, *ACS Photon.* **2**, 1769 (2015).
- [74] H. Vincent, D. Leroux, D. Bijaoui, R. Rimet, and C. Schlenker, *J. Solid State Chem.* **63**, 349 (1986).
- [75] A. F. May, Y. Liu, S. Calder, D. S. Parker, T. Pandey, E. Cakmak, H. Cao, J. Yan, and M. A. McGuire, *Phys. Rev. B* **95**, 174440 (2017).
- [76] F. Ye, M. Matsuda, Z. Morgan, T. Sherline, Y. Ni, H. Zhao, and G. Cao, *Phys. Rev. B* **106**, L180402 (2022).
- [77] K. Momma and F. Izumi, *J. Appl. Crystallogr.* **44**, 1272 (2011).
- [78] P. Blaha, K. Schwarz, G. K. Madsen, D. Kvasnicka, and J. Luitz, *WIEN2k*, An augmented plane wave+ Local Orbitals Program for Calculating Crystal Properties, edited by K. Schwarz (Vienna University of Technology, Austria, 2001).
- [79] J. P. Perdew, K. Burke, and M. Ernzerhof, *Phys. Rev. Lett.* **77**, 3865 (1996).
- [80] S. H. Vosko, L. Wilk, and M. Nusair, *Can. J. Phys.* **58**, 1200 (1980).
- [81] D. Koelling and B. Harmon, *J. Phys. C* **10**, 3107 (1977).
- [82] A. I. Liechtenstein, M. Katsnelson, V. Antropov, and V. Gubanov, *J. Magn. Magn. Mater.* **67**, 65 (1987).
- [83] X. Wan, Q. Yin, and S. Y. Savrasov, *Phys. Rev. Lett.* **97**, 266403 (2006).
- [84] X. Wan, T. A. Maier, and S. Y. Savrasov, *Phys. Rev. B* **79**, 155114 (2009).
- [85] D. Wang, X. Bo, F. Tang, and X. Wan, *Phys. Rev. B* **108**, 085140 (2023).
- [86] R. Kubo, *J. Phys. Soc. Jpn.* **12**, 570 (1957).
- [87] G. Grosso and G. P. Parravicini, *Solid State Physics* (Academic Press, New York, 2013).
- [88] F. Wooten, *Optical Properties of Solids* (Academic Press, New York, 1972).
- [89] J. Callaway, *Quantum Theory of the Solid State* (Academic Press, New York, 2013).
- [90] C. S. Wang and J. Callaway, *Phys. Rev. B* **9**, 4897 (1974).
- [91] P. M. Oppeneer, T. Maurer, J. Sticht, and J. Kübler, *Phys. Rev. B* **45**, 10924 (1992).
- [92] W. Feng, G.-Y. Guo, J. Zhou, Y. Yao, and Q. Niu, *Phys. Rev. B* **92**, 144426 (2015).
- [93] W.-K. Li and G.-Y. Guo, *Phys. Rev. B* **103**, 014439 (2021).
- [94] P. M. Oppeneer, Ph.D. thesis, Theoretische Physik Technische Universität Dresden, 1999.
- [95] M. Freiser, *IEEE Trans. Magn.* **4**, 152 (1968).
- [96] C. Robinson, *J. Opt. Soc. Am.* **54**, 1220 (1964).
- [97] T. Yoshino and S.-i. Tanaka, *Jpn. J. Appl. Phys.* **5**, 989 (1966).
- [98] T. Katayama, Y. Suzuki, H. Awano, Y. Nishihara, and N. Koshizuka, *Phys. Rev. Lett.* **60**, 1426 (1988).
- [99] P. Yang, W. Feng, G.-B. Liu, G.-Y. Guo, and Y. Yao, *Phys. Rev. B* **107**, 214437 (2023).
- [100] W. S. Werner, K. Glantschnig, and C. Ambrosch-Draxl, *J. Phys. Chem. Ref. Data* **38**, 1013 (2009).
- [101] V. Keast, *Micron* **44**, 93 (2013).
- [102] A. F. May, H. Cao, and S. Calder, *J. Magn. Magn. Mater.* **511**, 166936 (2020).
- [103] Y. Zhang, L.-F. Lin, A. Moreo, and E. Dagotto, *Phys. Rev. B* **107**, 054430 (2023).
- [104] D. Sangalli, A. Marini, and A. Debernardi, *Phys. Rev. B* **86**, 125139 (2012).
- [105] R. Lang, A. Winter, H. Pascher, H. Krenn, X. Liu, and J. K. Furdyna, *Phys. Rev. B* **72**, 024430 (2005).
- [106] G. Q. Di and S. Uchiyama, *Phys. Rev. B* **53**, 3327 (1996).